

Multiscale interactions within a multistage compressor

By P. J. Przytarski^{†‡}, M. Dellacasagrande[‡], M. Kozul[†],
R. Agrawal AND S. T. Bose[¶]

In this work, we employ proper orthogonal decomposition (POD) to quantify and characterize energy exchanges between various scales within a multistage compressor by utilizing the entire three-dimensional, unsteady flow field. A net estimate of the energy transfer rate between any two flow scales is computed, and a data-derived discrete energy cascade is constructed. This technique is then applied to cases with different levels of inflow unsteadiness, specifically as a result of the axial gap variation, in order to observe how inflow unsteadiness affects the interscale energy transfer.

1. Introduction

Turbomachinery flows feature complex interactions between stationary and rotating blades coupled with high levels of freestream turbulence. Figure 1(a) shows a flow field representative of a multistage compressor at a midspan section along with a spectrum obtained from a freestream probe embedded in a passage shown in pane (b) (Przytarski & Wheeler 2020). The computed spectrum shows a strong response from the upstream wakes with peaks at the blade passing frequency (BPF) and its harmonics. Further, a significant portion of the spectrum lies within the inertial subrange, with a considerable overlap between the inertial subrange and the BPF harmonics. This stands in contrast to typically made assumptions that some of the modeling methods rely on. Figure 1(c) shows a schematic sketch of an energy spectrum with conventional simulation paradigms (Sandberg & Michelassi 2019). In particular, standard modeling techniques, such as steady and unsteady Reynolds-averaged Navier-Stokes simulations (RANS/URANS), are likely to be unfit to reliably capture these effects, as the scales occupied by deterministic and stochastic disturbances are largely modeled, and their dynamics are lost. Despite these inherent limitations, RANS/URANS are widely used to develop and validate current engine designs (Slotnick *et al.* 2014). It is also known that flow unsteadiness, which is insufficiently modeled in these methods, can affect the performance of turbomachines (Folk *et al.* 2020).

In our previous work (Przytarski & Wheeler 2020), we performed high-fidelity simulations (see Figure 1) to characterize the unsteadiness within the multistage compressors and elucidate the mechanisms that increase unsteadiness via the interaction of deterministic and stochastic scales. For this purpose, we used a triple decomposition method in which the flow is split into a base flow, an oscillating wave and a stochastic flow field. However, this approach requires knowledge of a wave period and instantaneous phase angle, which may be inappropriate in flows with many wave-like dynamics. Instead, in this work, we use a data-driven flow decomposition method based on POD. This approach is

[†] Department of Mechanical Engineering, University of Melbourne, Australia

[‡] Department of Mechanical Engineering, University of Genova, Italy

[¶] Cadence Design Systems, Inc.

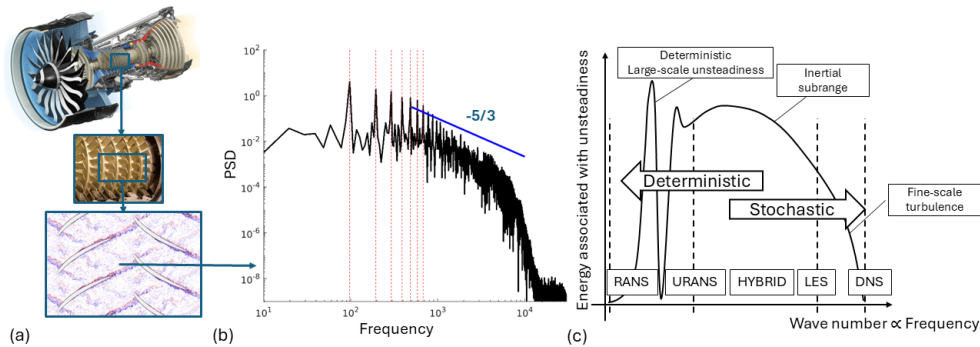


Figure 1: (a) An example flow field at a midspan section of a multistage compressor. (b) Turbulence power spectrum density (PSD) obtained from a high-fidelity simulation of an idealized multistage compressor, with red dashed lines corresponding to the blade passing frequency and its harmonics. (c) An approximate sketch of the turbulence spectrum, showing what portion of it various modeling techniques, such as large-eddy simulation (LES) and direct numerical simulation (DNS) aspire to resolve.

motivated by the need to better understand the multiscale nature of turbulence found within a multistage compressor flow field and to determine which scales are dynamically important and govern the flow of energy within the turbulence energy cascade. Identifying dynamically important scales is a departure from the conventionally made assumption of spectral equilibrium that classic turbulence modeling approaches make, in which all unresolved scales are characterized by a single length scale, (Schiestel 2008).

This analysis is the first step toward characterizing different scales within a multistage compressor flow field. To this end, the rest of this report attempts to address the following questions:

- (1) How do the interscale energy transfers govern the flow of kinetic energy in a multistage compressor?
- (2) How does the level of inflow unsteadiness affect these energy transfers?

In the following sections, we introduce the computational setup (Section 2) and the flow decomposition framework (Section 3). Then, we demonstrate the computation of the energy transfer rates and their reduction (Sections 4 and 5). Section 6 presents the impact of inflow conditions. Finally, some modeling outlooks and conclusions are offered in Section 7.

2. Computational setup

As mentioned before, we use the unsteady data of Przytarski & Wheeler (2020) for the controlled diffusion airfoil (*CDA*) blade profile. These data represent a compressor bladerow embedded in a multistage environment and were generated using the high-order compressible Navier-Stokes flow solver *3DNS* (Wheeler *et al.* 2018). For the cases considered here, all compressor blades were simulated in their on-design condition, i.e., 0° incidence. The Reynolds number based on the freestream velocity and the axial chord (C_{ax}) was $Re = 250000$, and the Mach number was 0.20. Figure 2(a) shows a schematic of the computational mesh and multiblock structure used in these computations. Approximately 170 million computational grid points were used. The simulation was run with a spanwise extent of 15% of the axial chord and periodic boundary conditions were applied

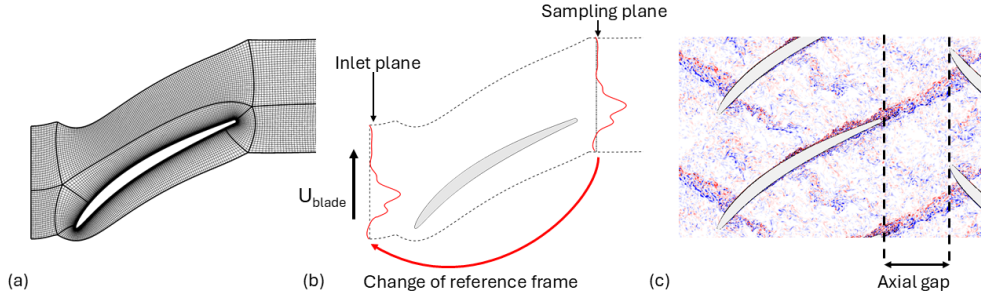


Figure 2: Summary of the simulation setup with (a) a baseline mesh showing every eighth line, (b) a schematic of the wake recycling procedure that mimics an idealized multistage environment and (c) an example flow field obtained from the simulation showing the definition of the axial gap, a parameter of interest that will be considered later in the report.

along the span. Further details regarding the resolution and simulation parameters can be found in Przytarski & Wheeler (2020).

The multistage environment was achieved using an idealized repeating-passage compressor model shown in Figure 2(b). In this model, the vortical disturbances are collected at the sampling plane, decomposed using a Fourier transform and reconstructed at the inlet using $N_y/2$ Fourier modes, where N_y is a pitchwise resolution. These inflow fluctuations are superimposed onto the mean inflow conditions via characteristic boundary conditions. More details of the model can be found in Przytarski & Wheeler (2020). Figure 2(c) shows an example of an instantaneous spanwise vorticity field for the *CDA* profile with a $0.4C_{ax}$ axial gap. In this figure, a single passage flow simulation was translated and reflected to reconstruct a full multistage picture, highlighting the validity of the idealized repeating-passage compressor model.

3. Large-scale flow decomposition

Standard flow decomposition approaches based on phase averaging provide a partial statistical representation of the flow complexity and may confound dynamics that are rare or not strictly periodic. Alternatively, we may use POD, first introduced by Lumley (1970). Given N observations of a velocity field $\underline{u}(\underline{x}, \tau)$, POD provides spatial modes $\phi(\underline{x})$, resembling flow structures, and temporal coefficients $\chi(\tau)$ retaining the mode dynamics. The POD modes and coefficients constitute two orthogonal bases for the velocity field $\underline{u}(\underline{x}, \tau)$. Accordingly, the i^{th} velocity component ($i \in \{1, 2, 3\}$) can be expressed as a linear combination of the modes

$$u_i(\underline{x}, \tau) = \sum_{l=1}^N \phi_i(\underline{x})^l \chi_l(\tau), \quad (3.1)$$

The POD coefficients computed herein are the eigenvectors of the temporal cross-correlation matrix, Q , of flow observations [also see Sirovich (1987)]. In this process, variables are stacked in the matrix M , whose columns contain the velocity components \mathbf{u}_i at all posi-

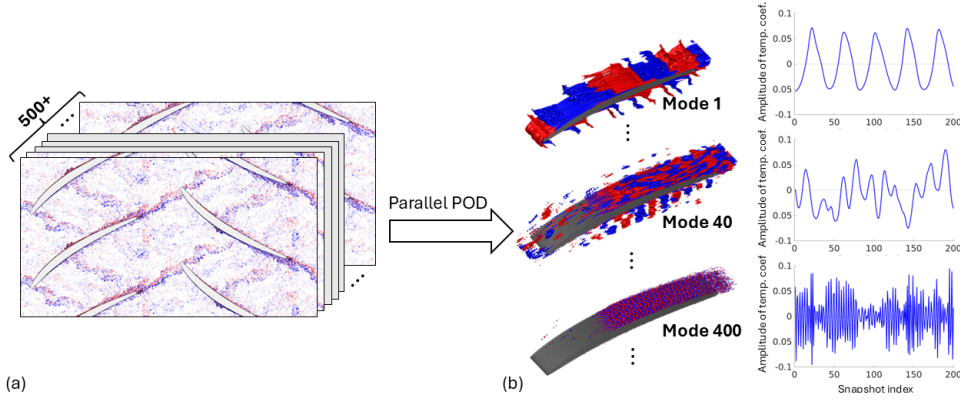


Figure 3: A schematic of a large-scale decomposition performed as part of this study in which (a) 500 3D snapshots comprising three velocity components are fed into an in-house parallel POD procedure and (b) a set of orthogonal spatial modes and corresponding temporal coefficients is obtained.

tions (\underline{x}_1 up to \underline{x}_p) and at a fixed time instance. Thus, M is constructed as

$$M = \begin{pmatrix} u_1(\underline{x}_1, \tau_1) & \cdots & u_1(\underline{x}_1, \tau_N) \\ \vdots & \ddots & \vdots \\ u_1(\underline{x}_{N_p}, \tau_1) & \cdots & u_1(\underline{x}_{N_p}, \tau_N) \\ u_2(\underline{x}_1, \tau_1) & \cdots & u_2(\underline{x}_1, \tau_N) \\ \vdots & \ddots & \vdots \\ u_2(\underline{x}_{N_p}, \tau_1) & \cdots & u_2(\underline{x}_{N_p}, \tau_N) \\ u_3(\underline{x}_1, \tau_1) & \cdots & u_3(\underline{x}_1, \tau_N) \\ \vdots & \ddots & \vdots \\ u_3(\underline{x}_{N_p}, \tau_1) & \cdots & u_3(\underline{x}_{N_p}, \tau_N) \end{pmatrix}, \quad (3.2)$$

where $u_{1,2,3}$ are the axial, pitchwise and spanwise velocity components, respectively, and N_p is the number of grid points. The POD temporal coefficients $\chi(t)$ are obtained from the solution of the following eigenvalue problem

$$QX = \Lambda X, \quad (3.3)$$

where $Q = M^T M$, X is the matrix containing the eigenvectors of Q and Λ is a diagonal matrix with sorted eigenvalues. Then, the POD mode matrix is computed as

$$\Phi = MX. \quad (3.4)$$

The distributed POD procedure of Biassoni *et al.* (2024) is used in this work. This procedure relies on Python's Dask library to parallelize the computations. First, the snapshots are read in parallel and the velocity components are extracted and stored in memory. Instead of constructing one matrix M that contains the entire data set, the procedure divides the dataset into N_k blocks that are processed in parallel. Each block k contains all the N_t snapshots, but only a subset of points within the domain: $N_{p,k}$ with each point consisting of all three velocity components, thus forming a matrix M_k . For each such block k , a cross-correlation matrix Q_k is calculated by computing the matrix

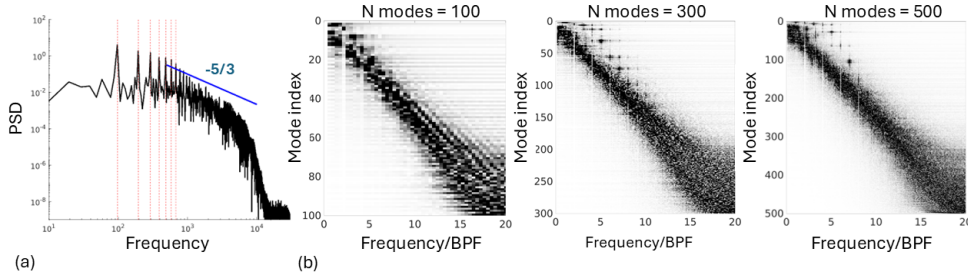


Figure 4: The sensitivity of the flow decomposition to the amount of data: (a) a turbulence spectrum obtained from a probe within the simulation flow field and (b) spectrograms obtained by computing a Fourier transform of temporal coefficient signals using 100, 300 and 500 snapshots.

product of M_k^T and M_k . The cross-correlation matrices Q_k are then summed to obtain the final cross-correlation matrix Q related to the entire computational domain. Finally, this matrix is fed into a singular value decomposition algorithm that returns eigenvalues and eigenvectors. The full matrix M is also saved to a disk using Parquet, a distributed data format, which is essential for the computation of transfer rates (described later). The details of this procedure and its performance are reported in Biassoni *et al.* (2024). For illustrative purposes, Figure 3 shows an application of the described procedure using 500 3D snapshots, each consisting of $170M$ coordinates with three velocity components. This corresponds to approximately 250 billion points. The computation took approximately 3 hours on four CPU nodes. Figure 3(b) shows example POD modes and the corresponding temporal coefficients.

In Figure 4, we investigate the sensitivity of this procedure to the number of chosen snapshots by inspecting the spectrograms obtained by computing a Fourier transform of temporal coefficient signals [shown in Figure 3(b)]. As expected, the spectrograms become more compact as the number of snapshots increases. For comparison, we also include the spectrum obtained from the freestream probe, Figure 3(a). Both, the freestream spectrum and the spectrograms, feature a strong signature of BPF and its harmonic as well as exhibit broadening of the spectrum towards the fine-scales. Generally, it can be concluded that both the spectrum and the spectrograms carry strong qualitative resemblance.

Figure 4 (b) demonstrates that, generally, POD separates the modes related to BPF and its harmonics relatively well. The results also suggest that at least 300 snapshots are needed to isolate BPF-related modes. The figure also demonstrates that POD modes exhibit a relatively small spread of frequencies. It is also clear that the frequencies increase approximately linearly with the mode number, up to the point where the mode coherence is lost and the spectrogram broadens (bottom right corner).

4. Kinetic energy transport equation and transfer of energy

Existing decompositions, such as the Reynolds or Hussain-Reynolds decompositions, estimate the coupling and the energy flow between the mean and turbulent fields via turbulence production and transfer rate terms that are part of the kinetic energy budget. In the context of POD, the velocity field can be represented as $\mathbf{u} = \bar{\mathbf{u}} + \sum_l \tilde{\mathbf{u}}^l$, where $\bar{\mathbf{u}}$ is a time mean of a velocity vector, and $\tilde{\mathbf{u}}^l$ is a velocity vector of a scale associated with

a particular POD mode. In this work, we follow the derivation of Baj & Buxton (2017) to determine the energy transfer rates. However, in contrast to the original derivation, in our work we omit the stochastic scale. Its absence is due to the nature of the POD which decomposes the flow only into a set of discrete modes and no stochastic scale is present. Consequently, the kinetic energy is defined as

$$K_{tot} = \frac{1}{2} \overline{u_i u_i} = \frac{1}{2} \bar{u}_i \bar{u}_i + \sum_l \frac{1}{2} \overline{\tilde{u}_i^l \tilde{u}_i^l} = \bar{k} + \sum_l \tilde{k}^l, \quad (4.1)$$

and the kinetic energy budget for all the scales within the flow is given as

$$\bar{\mathcal{L}} + \bar{\mathcal{C}} = - \sum_l \tilde{\mathcal{P}}^l - \bar{\epsilon} + \bar{\mathcal{D}}, \quad (4.2a)$$

$$\tilde{\mathcal{L}}^l + \tilde{\mathcal{C}}^l = \tilde{\mathcal{P}}^l + \tilde{\mathcal{T}}_+^l - \tilde{\mathcal{T}}_-^l - \tilde{\epsilon}^l + \tilde{\mathcal{D}}^l, \quad (4.2b)$$

where

$$\begin{aligned} \bar{\mathcal{L}} &= \frac{\partial \bar{k}}{\partial \tau}, & \tilde{\mathcal{L}}^l &= \frac{\partial \tilde{k}^l}{\partial \tau}, & \bar{\mathcal{C}} &= \bar{u}_j \frac{\partial \bar{k}}{\partial x_j}, & \tilde{\mathcal{C}}^l &= \bar{u}_j \frac{\partial \tilde{k}^l}{\partial x_j}, \\ \tilde{\mathcal{P}}^l &= -\overline{\tilde{u}_i^n \tilde{u}_j^l} \frac{\partial \bar{u}_i}{\partial x_j}, & \tilde{\mathcal{T}}_+^l &= -\frac{1}{2} \sum_{m,n} \overline{\tilde{u}_i^l \tilde{u}_j^m} \frac{\partial \tilde{u}_i^n}{\partial x_j}, & \tilde{\mathcal{T}}_-^l &= -\frac{1}{2} \sum_{m,n} \overline{\tilde{u}_i^n \tilde{u}_j^m} \frac{\partial \tilde{u}_i^l}{\partial x_j}, \\ \bar{\epsilon} &= 2Re^{-1} \bar{s}_{ij} \bar{s}_{ij}, & \tilde{\epsilon}^l &= 2Re^{-1} \overline{\tilde{s}_{ij}^l \tilde{s}_{ij}^l}, \\ \bar{\mathcal{D}} &= \frac{\partial}{\partial x_j} \left(-\bar{p} \bar{u}_j - \sum_m \overline{\tilde{u}_i^m \tilde{u}_j^m} \bar{u}_i + 2Re^{-1} \bar{s}_{ij} \bar{u}_i \right), \\ \tilde{\mathcal{D}}^l &= \frac{\partial}{\partial x_j} \left(-\tilde{p}^l \tilde{u}_j^l - \frac{1}{2} \overline{\tilde{u}_i^n \tilde{u}_j^m \tilde{u}_i^l} + 2Re^{-1} \overline{\tilde{s}_{ij}^l \tilde{u}_i^l} \right), \\ \bar{s}_{ij} &= \frac{1}{2} \left(\frac{\partial \bar{u}_i}{\partial x_j} + \frac{\partial \bar{u}_j}{\partial x_i} \right), & \tilde{s}_{ij}^l &= \frac{1}{2} \left(\frac{\partial \tilde{u}_i^l}{\partial x_j} + \frac{\partial \tilde{u}_j^l}{\partial x_i} \right). \end{aligned}$$

The terms of particular interest are $\tilde{\mathcal{T}}_-^l$ and $\tilde{\mathcal{T}}_+^l$, which correspond to the extraction and insertion of energy between the l^{th} scale and the remaining scales, respectively.

5. Quantifying energy transfer within the turbulence cascade

To evaluate the energy transfer rates within the turbulence cascade, we follow the convention of Baj & Buxton (2017) and aggregate them into the triadic production term $\tilde{\mathcal{T}}_+^l - \tilde{\mathcal{T}}_-^l$ to evaluate the interscale energetic exchanges.

For notational purposes, let the triadic production between every triad of scales be defined as

$$T_{l,m,n} = -\overline{\tilde{u}_i^l \tilde{u}_j^m} \frac{\partial \tilde{u}_i^n}{\partial x_j} \quad i, j = 1, 2, 3. \quad (5.1)$$

According to Eq. (3.1), each term in Eq. (5.1) can be expanded as a product of modes l, m, n and respective temporal coefficients:

$$T_{l,m,n} = -\phi_i^l \phi_j^m \frac{\partial \phi_i^n}{\partial x_j} \frac{1}{N} \sum_{t=1}^N \chi_i(t)^l \chi_j(t)^m \chi_i(t)^n \quad i, j = 1, 2, 3. \quad (5.2)$$

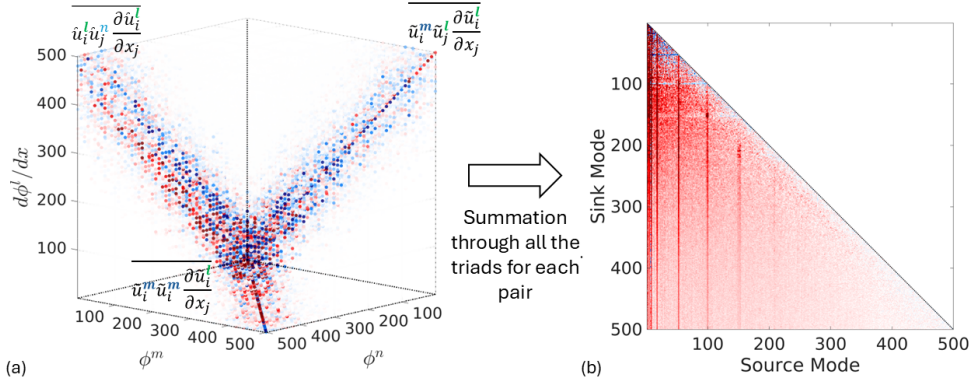


Figure 5: Estimation of transfer rates and construction of a data-derived discrete energy cascade showing (a) computation of all 500^3 transfer rates of a triadic nature within the flow field, displaying a strong diagonal alignment and (b) 2D reduction of transfer rates to represent a net transfer of energy between any pair of modes. Distinct vertical lines represent modes related to blade passing frequency and its harmonics and how they transfer energy and energize the scales across the entire spectrum.

Then, $T_{l,m,m}$ is integrated over the volumetric domain to determine the interscale energy transfer, $\mathcal{T}_{l,m,n}$, from scale (i.e., POD mode) n to l via scale m . Note that this relation suggests that the energy flow may occur between any triad of modes or that for every point in the $170M$ mesh, there are $N^3 = 500^3$ potential interactions, totaling over 2×10^{16} individual energy transfers. We use an in-house Python framework with the Dask library for these computations. The data are first read from the Parquet data format and, as before, partitioned into blocks. Each block constructs a partial data set matrix M_k that consists of three velocity components for a small subsection of a domain and all the snapshots for that subsection. Then, a matrix product between the partial data set matrix M_k and the eigenvector matrix X is performed to obtain the partial POD modes Φ^k . Each block fixes the source mode n and computes the spatial derivatives of it. Subsequently, the matrix product between all the partial POD modes Φ^l , all the partial POD modes Φ^m and the spatial derivatives of a fixed mode ϕ_n is computed. This computation is weighted by the domain volume to result in a volume integral value and repeated for every mode n to obtain the final 3D matrix. Finally, this matrix is multiplied by a triple product of temporal coefficient matrix χ to obtain the full energy transfer rate. For reference, these computations took approximately 20 hours using twelve CPU nodes.

Figure 5(a) presents the results from this computation as a 3D cube with mode indices corresponding to scales m , n and l on its axes. Each dot corresponds to a nonzero value of a volume integrated energy transfer rate between a particular triad of modes, with the color representing the direction of the energy flow: blue corresponds to a triad acting as an energy sink, and red corresponds to an energy source. We can observe that the nonzero components tend to fall along the diagonals. This corresponds to the triadic interaction for which one of the two scales acts also as an intermediate when the energy is exchanged between any pair of scales. Despite the apparent energy transfer tensor

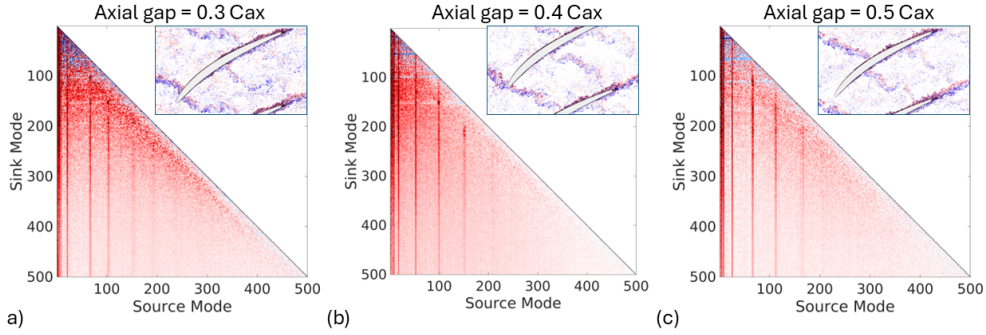


Figure 6: The impact of axial gap variation on the energy cascade showing how a shorter axial gap intensifies the energy transfers along the modes related to blade passing frequency as well as along the diagonal showing an increased role of inertial subrange in redistributing turbulence kinetic energy.

sparsity, the physical interpretation of the energy flow based on the the Figure 5 (a) is still challenging.

To overcome this, we evaluate the net energy transfer between any two given scales (POD modes), l and n as

$$\mathcal{T}_{l,n} = \sum_m \mathcal{T}_{l,m,n}. \quad (5.3)$$

Further, to avoid computation of two-way transfer rates in which energy is exchanged from scale l to n and from scale n to l , we sum these exchanges by choosing a preferential transfer direction, i.e., from a lower-order scale (POD mode) to a higher-order scale. Figure 5(b) presents the results of this summation, where the red color indicates a net flow of energy toward the higher frequencies (higher-order POD modes). Energy backscatter is represented by the negative values of $\mathcal{T}_{l,n}$. The figure shows that energy flows primarily down the turbulence cascade and that the energy exchanges are dominated by the lower-order modes, which tend to energize higher-order modes in their spectral vicinity. The vertical lines show that the BPF and its harmonics energize the entire turbulence spectrum, including the smallest flow scales. This holds true even for the higher-order harmonics (mode number equal to approximately 150). A non-negligible amount of backscatter is also found within the energy cascade, but appears to be generally confined to the first 50 modes.

6. The impact of inflow conditions

Next, we apply the present POD framework to two additional inflow conditions to assess how generalizable this dynamical picture of the energy flow is. These additional data sets were obtained in a similar way as the one described previously, except for the distance between the inlet and the blade's leading edge to represent a compressor with a shorter/longer interrow spacing, i.e., a compressor that is more or less compact.

Figure 6 shows the energy cascade for three cases with different axial gap configurations. For consistency, all the cases were analyzed in an identically manner. The energy

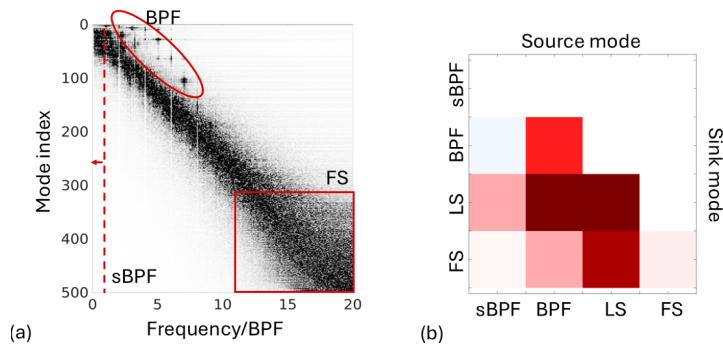


Figure 7: An example of manual classification of modes, splitting them based on their spectral content (a) into modes related to blade passing frequency (BPF), modes with strong sub-blade passing frequency response (sBPF) and less coherent scales for which the spectrum broadens [fine-scales (FS)]. The remaining scales are grouped together [large-scales (LS)]. (b) The resulting reduction of the discrete energy cascade in a 4×4 transfer rate matrix.

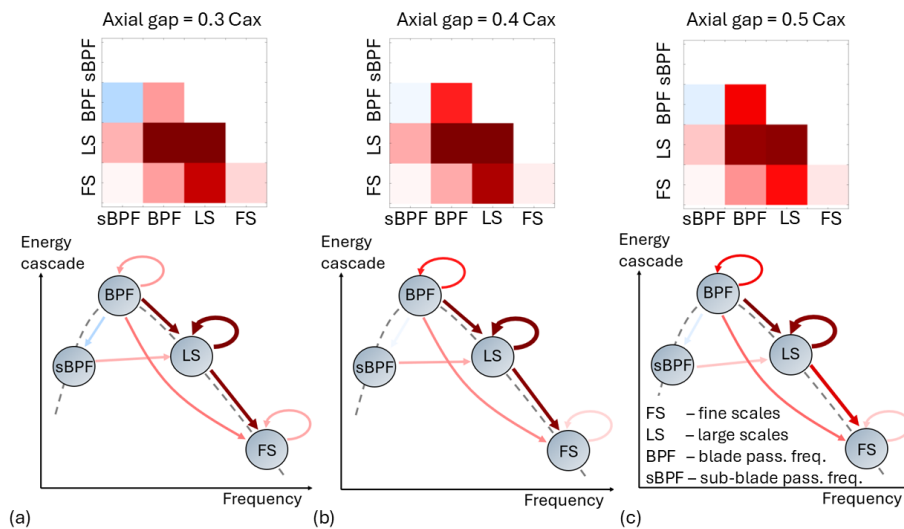


Figure 8: A phenomenological representation of a turbulence spectrum using previously established manual classification for three axial gaps of (a) 0.3, (b) 0.4 and (c) 0.5 axial chord.

cascades show strong qualitative similarity. In all three cases, modes that are related to BPF and its harmonics dominate the energy cascade. Majority of the significant transfer rates is limited to the lower-order modes. However, for the short axial gap case (with higher unsteadiness), high energy transfer rate values extend deeper into the energy cascade, suggesting a richer and more complex dynamical picture that is likely to feature stronger interactions between the individual dynamics.

7. Modeling Outlook and Conclusions

The main difficulty in translating these results into modeling insights is their complexity. Even if the role of the modes related to BPF and its harmonics is clear, what is unclear is how this knowledge can be utilized for better turbulence modeling. In principle, all modes can be treated separately, and the entire data-derived turbulence cascade could be turned into a turbulence model as is, but keeping track of 500 coupled turbulence equations is a significant departure from the current two-equation turbulence model standard.

One possible approach toward reducing this problem is mode classification. In Figure 7(a), we show an example manual classification of modes based on the spectral content of their temporal coefficients. The proposed classification is simple and illustrates a proof of concept. The modes are split into four families related to sub-blade passing frequency, blade passing frequency and its harmonics, large-scale dynamics and fine-scale dynamics. The mode families are self-explanatory with an exception of the split between large- and fine-scale dynamics, which are delineated by the broadening of the spectrogram.

This allows us to reduce the energy cascade shown in Figure 5 (b) and obtain a 4×4 transfer rate matrix. As a result we can represent the spectrum phenomenologically for the three considered axial gap flows as shown in Figure 8. The figure shows that there is a transfer of energy occurring from BPF dynamics into sub-BPF, especially as the gap is decreased and the inflow unsteadiness increases, signifying a potential mechanism for the emergence of sub-BPF dynamics.

As more cases are gathered and analyzed, a generalizable, more refined, phenomenological dynamic picture of turbulence may arise. This information could be used to construct data-informed sub-grid scale models for LES. These models could be also reformulated and adopt the form of ordinary differential equations to embed some of the missing sub-grid scale dynamics in them. It is also envisaged that this analysis will help formulate multi-scale turbulence transport models for RANS applications and this reduction will form a basis for the transport equation coupling.

Acknowledgements

P.J. Przytarski acknowledges funding from the European Union's Horizon 2020 research and innovation program under the Marie Skłodowska-Curie grant agreement No [101026928]. We also acknowledge ISCRA which awarded access to CINECA resources.

REFERENCES

- BAJ, P. & BUXTON, O. R. H. 2017 Interscale energy transfer in the merger of wakes of a multiscale array of rectangular cylinders. *Phys. Rev. Fluids* **2**, 114607.
- BIASSONI, D., RUSSO, M., VIVIANI, P., VITALI, G. & LENGANI, D. 2024 A high-performance code for analyzing loss transport equations in high-fidelity simulations. *Proceedings of ASME Turbo Expo* **12C**, V12CT32A039.
- FOLK, M., MILLER, R. J. & COULL, J. D. 2020 The impact of combustor turbulence on turbine loss mechanisms. *J. Turbomach.* **142**, 091009.
- LUMLEY, J. L. 1970 Stochastic Tools in Turbulence. *Academic Press* .

- PRZYTARSKI, P. J. & WHEELER, A. P. S. 2020 The effect of gapping on compressor performance. *J. Turbomach.* **142**, 121006.
- SANDBERG, R. D. & MICHELASSI, V. 2019 The current state of high-fidelity simulations for main gas path turbomachinery components and their industrial impact. *Flow Turb. and Combust.* **102**, 797–848.
- SCHIESTEL, R. 2000 *Modeling and Simulation of Turbulent Flows*. John Wiley & Sons.
- SIROVICH, L. 1987 Turbulence and the dynamics of coherent structures. I Coherent Structures. *Quart. Appl. Math.* **45**, 561–571.
- SLOTNICK, J., KHODADOUST, A., ALONSO, J., DARMOFAL, D., GROPP, W., LURIE, E. & MAVRIPLIS, D. 2014 CFD vision 2030 study: a path to revolutionary computational aerosciences. No. *NF1676L-18332*.
- WHEELER, A. P. S., DICKENS, A. M. J., & MILLER, R. J. 2018 The effect of nonequilibrium boundary layers on compressor performance. *J. Turbomach.* **140**, 101003.